

Coexistence of resistance switching and negative differential resistance in α -Fe₂O₃ nanorod film

Y. Y. Cai,^a Q. L. Yuan,^{a,b} Y. X. Ye,^a J. Liu^a and C. H. Liang^{*a}

^aKey Laboratory of Materials Physics and Anhui Key Laboratory of Nanomaterials and Nanotechnology, Institute of Solid State Physics, Chinese Academy of Sciences, Hefei 230031, China. E-mail: chliang@issp.ac.cn

^bDepartment of Materials Science and Engineering, University of Science and Technology of China, Hefei 230026, China.

Abstract: We report the coexistence of resistance switching (RS) behavior and negative differential resistance (NDR) phenomenon in α -Fe₂O₃ nanorod film grown in situ on fluorine-doped tin oxide glass substrate. The reversible switching of the low- and high-resistance states (LRS and HRS, respectively) of the film device can be excited simply by applying bias voltage. The switching from HRS to LRS was initiated at the negative bias region, whereas the NDR process followed by the reversion of HRS occurred at the positive bias region. With the increase in compliant current (CC), the carrier conduction models of LRS and HRS both changed and the current–voltage (I–V) relationships at the NDR region were seriously affected by the thermal process according to the level of applied CC. The co-existence of RS and NDR was possibly caused by defects during migration, such as oxygen vacancies and interstitial iron ions, which were formed in the α -Fe₂O₃ nanorod film. This work provided information on the ongoing effort toward developing novel electrical features of advanced transition metal oxide devices.

Keywords: resistance switching, negative differential resistance, α -Fe₂O₃ nanorods film, defects, thermal process

Introduction

The application of transition metal oxides (TMOs) exhibiting resistance switching (RS) potential in solid-state memory technology has attracted considerable interest. Although two basic models (bipolarity and unipolarity) that describe the RS features of these memories exist, some unusual transport behaviors in TMOs could still arise, such as the co-occurrence of bipolar and unipolar RS in ZnO¹ and the coincidence of memory and threshold RS in NiO.² These cases suggest that the RS features of TMOs have not yet been exhaustively defined. Another remarkable situation in TMOs is the coexistence of RS and negative differential resistance (NDR), indicating the abrupt mutation of resistivity or conductivity. NDR usually happens in III–V compound semiconductors or II–VI chalcogenide semiconductors according to intervalley carrier transfer theory.^{3,4} NDR has already been widely applied in a wide range electronic devices, such as resonant tunneling transistors,⁵ frequency multipliers,³ and high-frequency oscillators.⁶ Quite so, it's quite anticipated to develop such phenomenon to further improve memory application potential of TMOs after some reported literatures.^{30,31} However, the occurrence of NDR in TMOs and its correlation with RS behavior remain puzzling.

In TMOs, NDR often shows an “N”-shaped RS test results.^{7–9} The emergence of NDR indicates that current first increases with rising voltage before the peak voltage (V_P) is achieved, then drops down to the lowest value at the valley point voltage (V_V), and finally increases again with the continuously increasing voltage. This phenomenon is apparently the “Reset” step in RS (rapid switching from LRS to HRS). However, the current for NDR does not directly drop to HRS; rather, it decreases slowly and then increases again, which can be imaged as an incomplete “Reset” process or as an intermediate state between LRS and HRS. Studies^{7–9} have shown that the current can eventually revert to HRS following such an incomplete “Reset” process to ensure the duplication of RS behavior in successive voltage sweeping cycles. However, due to the great variability in electrical properties of TMOs induced by external means, the possible underlying mechanisms in this class of

oxides could be surprisingly different.³² Whether NDR really benefits the stability and sustainability of RS behavior remains inconclusive.

A currently attractive issue is that some crystallized TMOs, which are well known as candidates for nonvolatile memory in amorphous state, show a potential vista wherein NDR could benefit in realizing and enriching the RS functions in designing nanodevices. For instance, Ito et al. fabricated ZnO nanocrystal film exhibiting a double Schottky barrier structure to generate NDR phenomenon to tune the RS properties of a single-electron device.¹⁰ Chuang et al. also found that the NDR in the wurtzite ZnO nanorod can result in the breakdown of high current at an on-off current ratio of up to 10^6 .¹¹ In addition, Ziegler et al. have proven that, with the coordination of NDR, the crystalline TiO₂ film can display a stable bipolar RS characteristic even at the atomic scale.¹² Revealing the mechanism of NDR in various materials to clarify the correlation between NDR and RS behavior in TMOs has become an extremely important endeavor. Some theories associated with defects (e.g., grain boundary, dislocation, and vacancy) have been proposed; these theories include the resonant tunneling conduction of charges¹³ and the current in oxygen vacancies migration etc.⁷ These results show that the emergence of NDR in TMOs and its mechanism of action are closely related to the microscopic structures of TMOs themselves.

α -Fe₂O₃ (hematite), which is famous for its low cost, high safety, easy preparation, and good stability, exist in a wide range of electronic devices, such as gas sensor¹⁴ and field emitter.¹⁵ Moreover, α -Fe₂O₃ is compatible with various substrates (Si, conductive glass, etc.)¹⁶ and thus is a potential candidate material for advanced devices. Although amorphous iron oxides (Fe₂O₃, FeO_x) usually exhibit unipolar RS characteristics,^{17,18} the current-voltage (I-V) property of the crystallized α -Fe₂O₃ remains limited to Mott insulator,¹⁹ and its electrical conductive properties are unstable resulting from the change in external pressure or temperature. The influence of varied external biases to the internal structure of crystal lattice has been rarely reported. The latest report demonstrated that the Ga-doped α -Fe₂O₃ displays magnetic field-induced NDR,²⁰ however, the characteristics of pure α -Fe₂O₃ film under changed external bias is unknown.

This work initially reports on the coexistence of RS and NDR behaviors in well crystallized α -Fe₂O₃ nanorod film prepared through hydrothermal treatment of the fluorine-doped tin oxide (FTO) substrate in FeCl₃ solution followed by annealing at 550 °C in air.²¹ The impact of compliant current (CC) levels and voltage ranges on the I-V properties of the nanorod film were both investigated. The synthesized film displayed RS ON behavior at the negative bias region and NDR phenomenon at the positive bias region. At the NDR region, the current drastically dropped to nearly high-resistance state (HRS) under high CC levels, whereas it gently dropped to an intermediate state between HRS and low-resistance state (LRS) under low CC levels. The underlying mechanisms of NDR, which is closely related with the inevitable occurrence of defects in the growth film, are discussed herein. This work is the pioneering research on special I-V properties correlated with NDR in α -Fe₂O₃ nanorod film.

Experimental

The FTO glass substrate was placed in 25 mL of 0.05 mol/L FeCl₃ and 0.25 mol/L NaNO₃ aqueous solutions for hydrothermal treating at 120 °C for 3 h. The as-formed thin yellow-colored β -FeOOH nanorods film on the substrate must be washed with deionized water and ethyl alcohol by an ultrasonic washer to remove residual ions. The substrate then endured annealing at 550 °C for 2 h to get the final α -Fe₂O₃ nanorods film.

Field-emission scanning electron microscope (FESEM) (Sirion 200 FRG), transmission electron microscopy (TEM) (JEOL, JEM-2010), X-ray diffraction (XRD) (a Philips X'pert Pro diffractometer with Cu K _{α} radiation) were separately used to observe the morphologies, distinguish the fine structure and determine the crystalline information. Top tungsten (W) electrodes with 25 μ m in diameter were deposited via the small ion sputtering (SBC-12, KYKY, Beijing). Current-voltage (I-V) measurement was performed with a semiconductor analyzer (Agilent B1500A). Temperature dependent resistance of the film was investigated by using four-probe method in a physical property measurement system (PPMS).

Results and discussion

Fig. 1 shows the basic characterizations of the as-formed α -Fe₂O₃ film. The top morphology in Fig. 1(a) shows the compacted nanorod film, whose average diameter was approximately 50 nm; the inset shows the image of the real specimen. Fig. 1(b) shows that the average thickness of the film on the FTO conductive glass substrate was approximately 420 nm. Fig. 1(e) shows a random nanorod, and Fig. 1(c) shows the high-resolution TEM image of a portion of the white wire frame of this single nanorod; the corresponding selected area electron diffraction (SAED) pattern (Fig. 1(d)) provided an identical structural information. Moreover, three kinds of lattice fringes existed; the interplanar spacing of these fringes was 0.253 nm and the angle between any two planes was 60°. These results were consistent with relationships among (110), ($\bar{1}$ 20), and (2 $\bar{1}$ 0) planes, which belonged to the {110} facets of the rhombohedral structure α -Fe₂O₃. The XRD pattern (Fig. 1(f)) also demonstrated that the partial diffraction peaks of the specimen are well indexed to rhombohedral hematite (JCPDS 33-0664), which exhibits the (110) plane as its second strongest diffraction peak, and the other peaks were well indexed to tin dioxide (SnO₂) (JCPDS 46-1088).

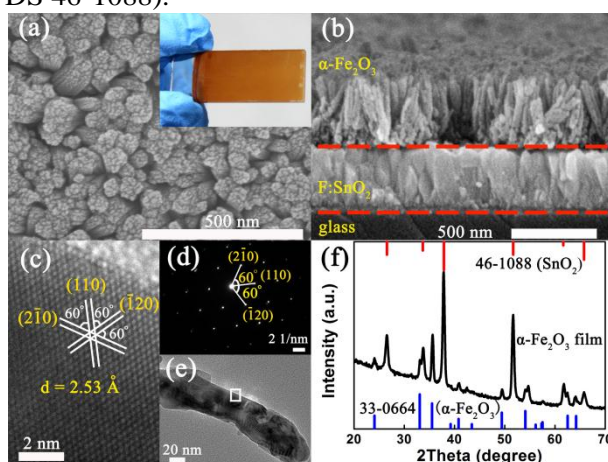


Fig. 1 Basic characterizations of the α -Fe₂O₃ nanorod film on FTO substrate: FESEM image of the (a) top and (b) side morphologies. (c) High-resolution image corresponding to the white wire frame part in (e). (d) SAED pattern corresponding to (e). (e) TEM image of a single nanorod. (f) XRD pattern of the film.

Fig. 2 shows the five consequent I–V sweeping curves under the CC levels 10 and 14 mA. The top W electrode displayed a positive bias at the beginning of the sweep. The sweeping order was as follows: $V_{\max} \rightarrow 0 \rightarrow -V_{\max} \rightarrow 0 \rightarrow V_{\max}$. Fig. 2(a) shows that at 10 mA CC, the current varied exponentially with voltage in HRS in step 1, which is consistent with the inherent semiconductor conductivity of the crystallized hematite. When the voltage swept across zero point and arrived at the region between -1.0 and -1.5 V in step 2, the current abruptly jumped to the CC limit, indicating the occurrence of the “Set” process, thereby facilitating the conversion from HRS to LRS. In step 3, the current varied with voltage in LRS nearly linearly. When the voltage swept to approximately $+0.85$ V in step 4, the current displayed a soft breakdown followed by slow rising to CC (see Fig. 2(c)); this incomplete “Reset” process indicated the existence of NDR. Finally, the conductivity was reversed to HRS, which completes one sweeping cycle. However, with CC rising up to 14 mA (Fig. 2(b)), the I–V curve was always of exponential or semiconductor-like form in HRS and LRS. The “Set” process also occurred between -1.0 and -1.5 V, although the current in step 4 would considerably drop to nearly HRS at approximately $+1.2$ V and nearly completely rupture at the NDR region (see Fig. 2(d)). To further investigate the influence of the current level, the CC value was changed from 2.5 mA to 16 mA (Fig. S1, see ESI†). The results confirmed that high CC (≥ 13 mA) would result in a more intensive breakdown of LRS and to high peak-to-valley current ratio. Moreover, we conducted a test to determine the effect of voltage range. Fig. S2 shows the comparison of the I–V curves

sweeping in different voltage regions (see ESI). At constant CC (e.g., 10 and 12 mA), nearly all curves overlapped. In addition, the absolute values of the voltages for the “Set” process and NDR peak were all lower than 2 V. Thus, the voltage range shows no visible effect. This work is the first to observe the coexistence of RS behavior with NDR phenomenon in pure α -Fe₂O₃ nanorod film under external bias.

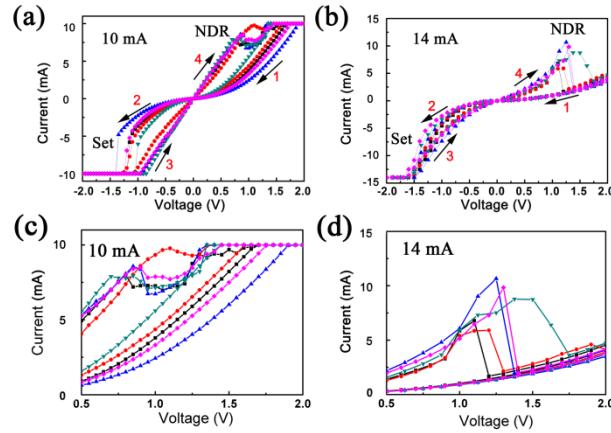


Fig. 2 I–V tests sweeping from +2 to –2 V and back to +2 V under different CC levels: (a) 10 mA and (b) 14 mA, magnified partial I–V curves in NDR region: (c) corresponding to 10 mA and (d) corresponding to 14 mA.

The plots of $\ln(I)$ versus $\ln(V)$ and of $\ln(I)$ versus $\text{Sqrt}(V)$ in Fig. 3 were fitted to illustrate the conduction mechanisms of the I–V curves in Fig. 2. When CC was set at 10 mA (Fig. 3(a)) whether in the positive or negative bias region in HRS, the slope was 1.23 at lower absolute value of voltage and rose to 2.06 at higher absolute value of voltage. This finding indicated that leaving the region of the “Set” process aside, the I–V relationship in HRS nearly obeyed the metallic conduction and then the space charge limited conduction (SCLC), which could be related to presence of defects (e.g., oxygen vacancies, dislocations, and voids).²² The slope of the I–V curve in LRS before sweeping to NDR peak voltage was 0.97, displaying a nearly metallic linear trend, which prefigured the existence of thermally generated carriers.²² The I–V relationships in Figs. 3(b) and 3(c) respectively corresponded to the HRS and LRS under 14 mA as CC. However, the logarithm of current in HRS was not linear with the logarithm of voltage but was linear with the square root of voltage. In addition, the slope values were 4.16 and 6.08 in the positive and negative bias regions, respectively. Thus, Schottky emission, which tended to appear at the interface aggregated with oxygen vacancies, is possibly the main transport mechanism.^{23,24} Note that the carriers should cross the potential barrier as facilitated by the thermionic effect under Schottky emission,²⁵ and this phenomenon was possible under a more intensive thermal effect at high CC levels. Fig. 3(c) shows the corresponding I–V relationships of LRS. In the negative bias region, the slope changed from 1.16 to 1.77 with increasing absolute voltage value. In the positive bias region, except for the NDR region, the slope of I–V curve changed from 1.09 to 1.50 and finally to 2.26 with increasing voltage. Thus, the carriers always followed the metallic conduction model and the Child’s law (SCLC) in LRS, and this situation was different from that under low CC. This observation further demonstrated the distinct characteristic of I–V relationships being dependent on CC values. According to the aforementioned description, the transport of conduction carriers should be largely related to thermal process determined by the current level.

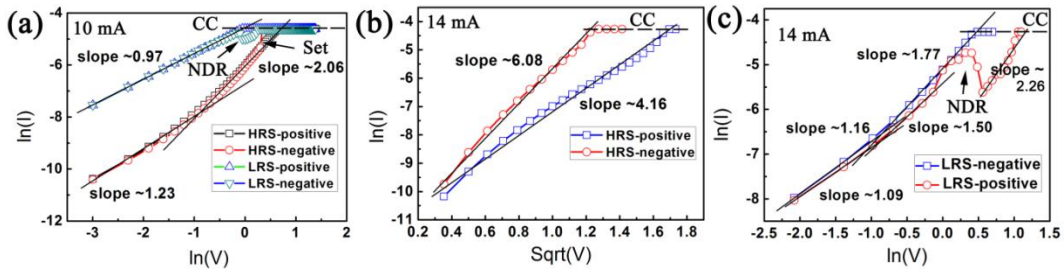


Fig. 3 (a) Double-logarithmic plots of the I–V curves in HRS and LRS at 10 mA CC. (b) Plot of $\ln(I)$ vs. $\text{Sqrt}(V)$ in HRS at 14 mA CC. (c) Plot of $\ln(I)$ vs. $\ln(V)$ in LRS at 14 mA CC.

Fig. 4 shows temperature dependence of resistance in HRS and LRS to further investigate the conduction mechanisms of carriers. CC was selected herein as 14 mA, under which the thermal effect was sufficiently severe. In HRS (black curve), the read voltage was set at +1.4 V, and the resistance dropped with increasing temperature from 150 K to 300 K. This finding illustrated that the semiconductor feature originated from the intrinsic conductivity of hematite. This finding is also consistent with the result shown in Fig. 2(b). In LRS, the resistance-temperature (RT) curves were read at +0.5 and +1.4 V outside (red curve) and within the NDR region (blue curve), respectively, to distinguish the difference between various states before and after NDR. The former curve indicated a weak semiconductor behavior for the relative resistance ratio defined as $R_{(300\text{ K})}/R_{(150\text{ K})}$ of 0.89, whereas the latter curve presented an apparent transition at approximately 260 K. The semiconductor feature of the blue curve changed from being faint to being strong with the abrupt increase in resistance to 260 K, indicating that the conduction mechanism changed according to the variations in temperature. At least two possible mechanisms could be considered at temperatures above 260 K, and one of them possibly collapsed at low temperature. Note that the major inevitable point defects in crystallized $\alpha\text{-Fe}_2\text{O}_3$ are oxygen vacancies and the interstitial Fe^{3+} or Fe^{2+} ions.²⁶ The phenomenon where oxygen vacancy brings about bipolar RS in metal oxides with unsymmetrical top and bottom electrodes are often observed.²⁷ However, notice that tunneling current was possibly induced by the hopping conduction of electrons between multivalent ions (e.g., Fe^{3+} or Fe^{2+}) in metal oxides; this conduction is thermally activated and will be localized at hopping sites as temperature decreases.²⁸ Herein, we expected the synergy of migration of oxygen vacancies and electron conduction between the hopping sites to result in better conductivity that is close to that of a conductor at temperatures above 260 K. The localization of hopping electrons would occur at temperatures lower than 260 K, resulting in higher resistance.

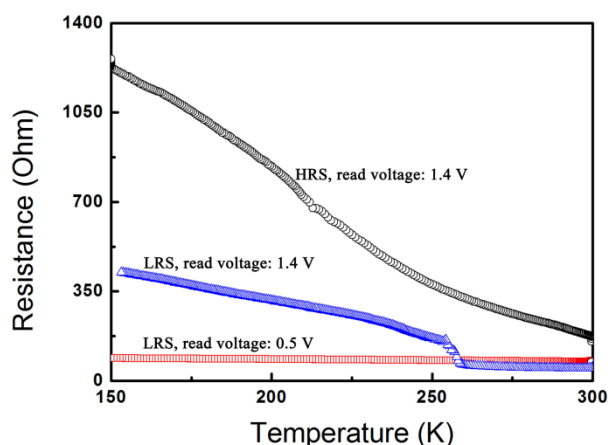
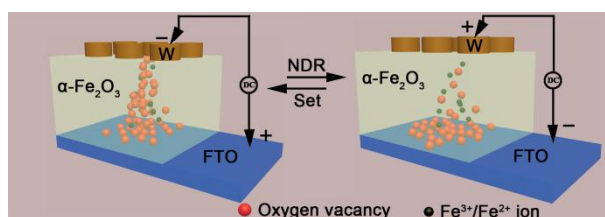


Fig. 4 Temperature-dependent resistance (RT) curves of the film structure at 14 mA CC.

Scheme 1 illustrates the possible mechanism of the oxygen vacancies and the hopping electrons between the interstitial $\text{Fe}^{3+}/\text{Fe}^{2+}$ ions excited by external bias. Oxygen vacancies usually easily accumulate at the interface of heterojunction (e.g., interface between oxide film and FTO substrate) resulting from the mismatch of stoichiometry and local strain.²³ At the beginning of voltage sweeping, the bottom FTO electrode was under negative bias and the positively charged oxygen vacancies tended to localize there. Only the thermally generated intrinsic carriers of hematite are transported into the film, leading to the exponential I–V relationship in HRS. After the voltage sweeping into the negative region, the oxygen vacancies gradually migrated into the top electrode and formed conducting filaments at the “Set” voltage. When bias returned to the positive zone, such filaments would rupture slowly resulting from the return of oxygen vacancies to the bottom electrode, leading to the piecemeal drop of current and cause the NDR peak. The RT test revealed that the thermal effect at room temperature was inevitable. The tunneling current formed by the hopping electrons would be activated with increasing Joule heat of the conducting filaments, possibly causing the current after NDR peak not to directly decrease to the low value of HRS. However, the activation energy, hopping routes, etc. are still unclear and must be elucidated in future work. By contrast, the current would decrease to nearly HRS under higher CC level. The compliance current could also determine the type of RS because the current level of the filaments determines the amount of Joule heat.^{1,24} Herein, the gentle breakdown of filaments under 10 mA CC was caused by the migration of oxygen vacancies to the bottom of FTO; however, further fusion of filaments at 14 mA CC should contribute to the excessively intensive thermal effect.



Scheme 1 Schematic of the formation and rupture of conducting filaments consisting of oxygen vacancies and hopping electrons between the interstitial $\text{Fe}^{3+}/\text{Fe}^{2+}$ ions in the configured W/ $\alpha\text{-Fe}_2\text{O}_3$ nanorod film/FTO sandwich structure.

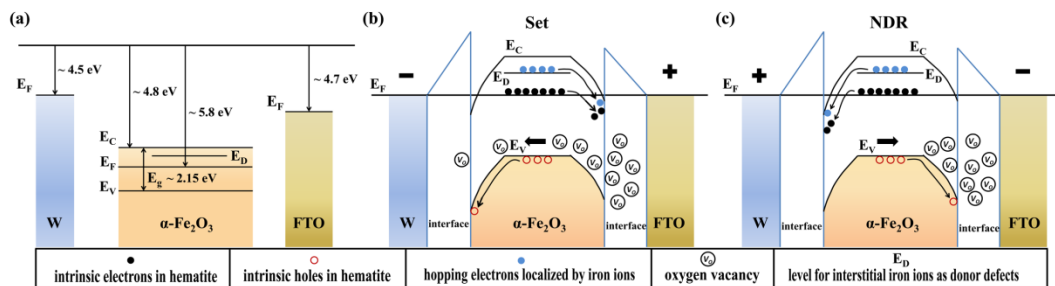


Fig. 5 (a) energetic alignments of EC, EV, EF levels of $\alpha\text{-Fe}_2\text{O}_3$ nanorod film, tungsten and FTO substrates. Possible band diagrams of W/ $\alpha\text{-Fe}_2\text{O}_3$ and $\alpha\text{-Fe}_2\text{O}_3$ /FTO interfaces in different processes: (b) “Set” process and (c) NDR process

In Fig. 5, we discuss a possible model of “Set” process and NDR behavior based on the energy band diagrams. Fig. 5(a) summarized possible energetic alignments of conduction band (E_C), valence band (E_V) and Fermi levels (E_F) of $\alpha\text{-Fe}_2\text{O}_3$ nanorod film.³³ The interstitial metal ions and oxygen vacancies are both considered as donor defects in n-type semiconductor metal oxides.^{34,35} The formation functions of oxygen vacancies and interstitial iron ions are shown in equation (S1) and equation (S2) in ESI. The donor levels (E_D) for interstitial $\text{Fe}^{3+}/\text{Fe}^{2+}$ ions and oxygen vacancies are both estimated between E_C and E_F . To avoid highly accumulation of carriers at E_D level in Fig. 5(b) and Fig. 5(c), oxygen vacancies are not shown in appropriately energetic location, but arranged according to real position (originally locate at the interface between $\alpha\text{-Fe}_2\text{O}_3$ nanorod film and FTO substrate). The E_F levels of tungsten and FTO electrodes are also listed in Fig. 5(a).³⁶ Due to the differences between E_F levels of the three materials which fabricate a sandwich structure, the energetic band of hematite at the two interfaces would bend until E_F levels attained equilibrium state. When the top W electrode was applied negative voltage in Fig. 5(b), the intrinsic electrons (major carriers) and holes (minor carriers) would be driven to FTO substrate and W electrode separately, and it gave rise to the exponential I–V relationship of semiconductor. Meanwhile, the hopping electrons between interstitial $\text{Fe}^{3+}/\text{Fe}^{2+}$ ions were driven to FTO substrate, while positive oxygen vacancies were impelled to W electrode. These carriers brought about the rapid enlargement of current and the final “Set” process. In Fig. 5(c), W electrode was applied positive voltage. All carriers changed their moving direction. Under lower CC, oxygen vacancies would go back to the interface between $\alpha\text{-Fe}_2\text{O}_3$ nanorod film and FTO substrate so as to the slight drop of current in NDR region. However, under higher CC, huge thermal effect would further destroy the conduction contribution from those hopping electrons between interstitial $\text{Fe}^{3+}/\text{Fe}^{2+}$ ions. So, a drastic dropping of current emerged in NDR region.

Although the I–V sweeping test could be replicated, the “Set” voltages and NDR peak voltages both slightly fluctuated (Fig. 2). This phenomenon is possibly caused by the incomplete rupture of the conductive paths during the NDR, which directly requires a mutable voltage to recover the filaments during the subsequent “Set” process.²⁹ Fig. S3 in ESI shows the fluctuating ranges of the “Set” and NDR voltages under various CC levels. The former ranged from -1.81 V to -0.55 V, whereas the latter ranged from +0.35 V to +1.87 V. However, the retention characteristics of the HRS and LRS were considerably stable. Fig. 6 shows the plots of current versus time for 10 min; the readout voltage was +0.5 V. Although the current ratio of LRS to HRS ($I_{\text{ON}}/I_{\text{OFF}}$) were only 8 and 3 under 10 and 14 mA, respectively, the I–t curves always remained constant during testing (Other I–t curves under different CC levels were provided in Fig. S4 in ESI).

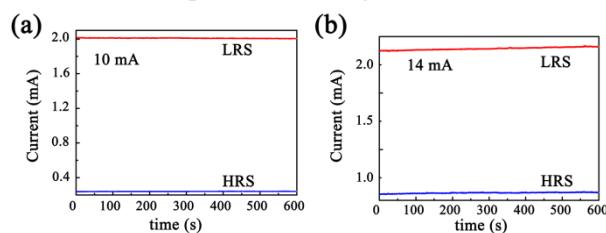


Fig. 6 Current-time curves of HRS and LRS read at +0.5 V under different CC levels: (a) 10 mA and (b) 14 mA.

Conclusions

The coexistence of RS and NDR in α -Fe₂O₃ nanorod film on FTO substrate prepared hydrothermally is reported herein for the first time. RS and NDR occurred under different polarities of applied voltage. The I–V curves demonstrated that LRS and HRS followed different conduction models and that they depended on the current levels, which directly affected the thermal process. We assumed that the observed phenomenon is related to the defects (oxygen vacancies, interstitial iron ions, etc.) in the α -Fe₂O₃ nanorod film. This work provides information on the electrical features of α -Fe₂O₃ nanorod films for low-cost production of efficient switching device.

Acknowledgements

This work was financial supported by the National Basic Research Program of China (2014CB931704), the National Natural Science Foundation of China (NSFC, No.51371166, 51571186, 11404338, 11304315, 51401206, 11504375) and China Postdoctoral Science Foundation.

References

- 1 S. Lee, H. Kim, J. Park and K. Yong, *J. Appl. Phys.*, 2010, **108**, 076101.
- 2 L. He, Z. M. Liao, H. C. Wu, X. X. Tian, D. S. Xu, G. L. W. Cross, G. S. Duesberg, I. V. Shvets and D. P. Yu, *Nano Lett.*, 2011, **11**, 4601.
- 3 Y. Q. Wu, D. B. Farmer, W. J. Zhu, S. J. Han, C. D. Dimitrakopoulos, A. A. Bol, P. Avouris and Y. M. Lin, *ACS Nano*, 2012, **6**, 2610.
- 4 B. Chitara, D. S. I. Jebakumar, C. N. R. Rao and S. B. Krupanidhi, *Nanotechnology*, 2009, **20**, 405205.
- 5 F. Beltram, F. Capasso, S. Luryi, S. G. Chu, A. Y. Cho and D. L. Sivco, *Appl. Phys. Lett.*, 1988, **53**, 219.
- 6 Y. F. Li, T. Kaneko and R. Hatakeyama, *J. Appl. Phys.*, 2009, **106**, 124316.
- 7 Y. Du, H. Pan, S. Wang, T. Wu, Y. P. Feng, J. Pan and A.T. S. Wee, *ACS Nano*, 2012, **6**, 2517.
- 8 A. L. Pergament, V. P. Malinenko, O. I. Tulubaeva and L. A. Aleshina, *Phys. Stat. Sol. A*, 2004, **201**, 1543.
- 9 F. Verbakel, S. C. J. Meskers, D. M. D. Leeuw and R. A. J. Janssen, *J. Phys. Chem. C*, 2008, **112**, 5254.
- 10 D. Ito, T. Tomita and T. Hatazawa, *Appl. Phys. Lett.*, 2007, **90**, 143118.
- 11 M. Y. Chuang, Y. C. Chen, Y. K. Su, C. H. Hsiao, C.S. Huang, J. J. Tsai and H. C. Yu, *ACS Appl. Mater. Inter.*, 2014, **6**, 5432.
- 12 M. Ziegler, O. Harnack and H. Kohlstedt, *SolidState Electron.*, 2014, **92**, 24.
- 13 D. Joung, L. Anjia, H. Matsui and S. I. Khondaker, *Appl. Phys. A*, 2013, **112**, 305.
- 14 Y. Wang, Y. M. Wang, J. L. Cao, F. H. Kong, H. J. Xia, J. Zhang, B. L. Zhu, S. R. Wang and S. H. Wu, *Sensor. Actuat. B*, 2008, **131**, 183.
- 15 Y. W. Zhu, T. Yu, C. H. Sow, Y. J. Liu, A. T. S. Wee, X. J. Xu, C. T. Lim and J. T. L. Thong, *Appl. Phys. Lett.*, 2005, **87**, 023103.
- 16 L. C. Hsu and Y. Y. Li, *Appl. Phys. Lett.*, 2008, **93**, 083113.
- 17 I. H. Inoue, S. Yasuda, H. Akinaga and H. Takagi, *Phys. Rev. B*, 2008, **77**, 035105.
- 18 S. B. Lee, S. C. Chae, S. H. Chang and C. Liu, *J. Korean Phys. Soc.*, 2007, **51**, S96.
- 19 J. Badro and G. Fiquet, *Phys. Rev. Lett.*, 2002, **89**, 205504.
- 20 R. N. Bhowmik and G. Vijayasri, *AIP Adv.*, 2015, **5**, 067126.
- 21 J. Liu, Y. Y. Cai, Z. F. Tian, G. S. Ruan, Y. X. Ye, C. H. Liang and G. S. Shao, *Nano Energy*, 2014, **9**, 282.
- 22 C. H. Liang, K. Terabe, T. Hasegawa and M. Aono, *Appl. Phys. Express*, 2008, **1**, 064002.
- 23 W. W. Li, R. Zhao, R. J. Tang, A. P. Chen, W. R. Zhang, X. Lu, H. Y. Wang and H. Yang, *ACS Appl. Mater. Inter.*, 2014, **6**, 5356.

-
- 24 B. S. Lee, B. Y. Kim, J. H. Lee, J. H. Yoo, K. Hong and S. Nahm, *Curr. Appl. Phys.*, 2014, **14**, 1825.
 - 25 W. Hu, L. L. Zou, R. Q. Chen, W. Xie, X. M. Chen, N. Qin, S. W. Li, G. W. Yang and D. H. Bao, *Appl. Phys. Lett.*, 2014, **104**, 143502.
 - 26 B. Amami, M. Addou, F. Millot, A. Sabioni and C. Monty, *Ionics*, 1999, **5**, 358.
 - 27 N. Xu, L. F. Liu, X. Sun, X. Y. Liu, D. D. Han, Y. Wang, R. Q. Han, J. F. Kang and B. Yu, *Appl. Phys. Lett.*, 2008, **92**, 232112.
 - 28 S. Witanachchi, H. Weerasingha, H. A. Mourad and P. Mukherjee, *Physica B*, 2010, **405**, 208.
 - 29 W. T. Lian, H. B. Lv, Q. Liu, S. B. Long, W. Wang, Y. Wang, Y. T. Li, S. Zhang, Y. H. Dai, J. N. Chen and M. Liu, *IEEE Electr. Device L.*, 2011, **32**, 1053.
 - 30 C. H. Jia, X. W. Sun, G. Q. Li, Y. H. Chen and W. F. Zhang, *Appl. Phys. Lett.*, 2014, **104**, 043501.
 - 31 G. Yang, C. H. Jia, Y. H. Chen, X. Chen and W. F. Zhang, *J. Appl. Phys.*, 2014, **115**, 204515.
 - 32 K. Szot, W. Speier, G. Bihlmayer and R. Waser, *Nat. Mater.*, 2006, **5**, 312.
 - 33 J. Zhang, X. H. Liu, L. W. Wang, T. L. Yang, X. Z. Guo, S. H. Wu, S. R. Wang and S. M. Zhang, *Nanotechnology*, 2011, **22**, 185501.
 - 34 Y. A. Sumanth, R. A. Sujatha, S. Mahalakshmi, P. C. Karthika, S. Nithiyanantham, S. Saravanan and M. Azagiri, *J. Mater. Sci: Mater. Electron.*, 2016, **27**, 1616.
 - 35 A. Sawa, *Mater. Today*, 2008, **11**, 28.
 - 36 Y. H. Zhou, J. W. Shim, C. F. Hernandez, T. M. Khan and B. Kippelen, *Thin Solid Films*, 2014, **554**, 54.